

Sensitized TiO₂ nanocomposites through HMME linkage for photodynamic effects

Yu Lu He
Sijia Wang
Luwei Zhang
Jing Xin
Jing Wang
Cuiping Yao
Zhenxi Zhang
Chih-Chung Yang

Sensitized TiO₂ nanocomposites through HMME linkage for photodynamic effects

Yu Lu He,^a Sijia Wang,^a Luwei Zhang,^a Jing Xin,^a Jing Wang,^a Cuiping Yao,^a Zhenxi Zhang,^{a,*} and Chih-Chung Yang^b

^aXi'an Jiaotong University, Key Laboratory of Biomedical Information Engineering of Education Ministry, Institute of Biomedical Analytical Technology and Instrumentation, School of Life Science and Technology, No. 28, Xianning West Road, Xi'an, Shaanxi 710049, China

^bNational Taiwan University, Institute of Photonics and Optoelectronics, No. 1, Section 4, Roosevelt Road, Taipei 10617, Taiwan

Abstract. Although TiO₂ can be used to effectively generate reactive oxygen species (ROS) for photodynamic application, its absorption in the ultraviolet range makes the excitation harmful to tissue. Based on the concept of a sensitized solar cell, TiO₂ nanoparticles (NPs) are sensitized by linking with the photosensitizer, HMME, to form HMME-TiO₂ nanocomposites (NCs) for demonstrating the photodynamic effects under the illumination of white light. The HMME-TiO₂ NCs of different composition ratios are prepared for maximizing the generation of ROS and optimizing the inactivation effect of KB cells. The material characteristics and the ROS generation capability of the HMME-TiO₂ NCs with the optimized combination ratio show their merits in a photodynamic process under white light irradiation. The application of such NCs to KB cell experiments results in a higher inactivation efficiency when compared to pure HMME of the same concentration. © 2016 Society of Photo-Optical Instrumentation Engineers (SPIE) [DOI: 10.1117/1.JBO.21.12.128001]

Keywords: sensitized TiO₂ nanoparticle; photodynamic therapy; daylight PDT.

Paper 160548R received Aug. 10, 2016; accepted for publication Nov. 21, 2016; published online Dec. 15, 2016.

1 Introduction

Photodynamic therapy (PDT) combines photosensitizer and light illumination for generating reactive oxygen species (ROS) to cause selective damage on targeted diseased tissue.^{1,2} A photosensitizer can be selectively accumulated in cancerous tissue. Upon light irradiation within its absorption spectrum, a photosensitizer absorbs photon energy and reacts with molecular oxygen, leading to the generation of ROS. During this process, the ROS generation efficiency of the photosensitizer and the excitation spectrum are two important factors. TiO₂ nanoparticles (NPs) have been widely used in sensitized solar cells and photocatalytic degradation of different pollutants by combining with photosensitizers.^{3–10} A photosensitizer can effectively absorb sunlight for transferring energy into TiO₂ and hence generating electron–hole pairs in a solar cell. TiO₂ NPs can also be used to produce ROS for the photodynamic process in tumor treatment.^{11–17} However, its absorption in the ultraviolet range makes its direct application to PDT impractical. Similar to the concept of a sensitized solar cell, TiO₂ NPs can be linked with a photosensitizer such that they can be excited by visible light through the absorption of the photosensitizer for PDT application. Although such a technique has been demonstrated, the cancer cell inactivation efficiency was not significantly improved.^{18,19} If the sensitized TiO₂ nanocomposites (NCs) can effectively absorb visible light of a broad spectrum, they can be used for daylight PDT. Photodynamic and photothermal effects for tumor treatment based on near-infrared laser illumination of surface-modified or hydrogenated TiO₂ NPs have been reported.^{20–23} The application of a near-infrared laser for PDT to tumor treatment has the advantage of deeper tissue penetration and hence more

efficient therapy. However, the ultraviolet excitation of TiO₂ by near-infrared laser illumination relies on a process combining the up-conversion mechanism of a linked material and the transfer of ultraviolet energy from the up-conversion material into TiO₂.^{20–22} Such a complicated process requires delicate design and synthesis of the linked materials to TiO₂ NPs for achieving a high enough TiO₂ excitation efficiency. In this regard, linking a TiO₂ NP with a photosensitizer, which effectively absorbs visible light, for efficient TiO₂ excitation can be an alternative approach of great use.

The conventional clinic-based PDT is time-consuming and laborious for medical professionals and patients and requires special equipment that takes up space.²⁴ Furthermore, the major side effects of the conventional PDT include severe pain during the light irradiation process and posttreatment inflammatory skin reactions.²⁵ To solve these problems in the conventional PDT, using daylight as the light source of PDT has been proposed.^{26–30} Using daylight as the PDT light source not only can simplify the treatment process but also can reduce pain because of the higher tolerance of humans to natural daylight.^{3,30,31} For daylight PDT development, the improvement of ROS generation efficiency based on a modification of the used photosensitizer, such as linking the photosensitizer onto a certain NP, for enhancing daylight PDT efficiency is an important research task.

In this paper, we report the fabrication of an NC by linking a photosensitizer onto a TiO₂ NP for enhancing white light absorption and ROS generation capability. Also, we demonstrate more effective photodynamic effects by using such NCs when compared with the case of pure photosensitizer. TiO₂ NP has been widely used as a regenerative photocatalyst that effectively absorbs ultraviolet light for generating cytotoxic hydroxyl

*Address all correspondence to: Zhenxi Zhang, E-mail: zxzhang@mail.xjtu.edu.cn

and superoxide radicals.³² Such a behavior of a TiO₂ NP makes it useful for serving as a photodynamic therapeutic agent.^{18,33–36} While ultraviolet light may damage human tissue, it has been shown that porphyrins as photosensitizers can effectively absorb light in the visible range.^{37,38} In this regard, the porphyrin-based photosensitizer HMME has been applied to the clinical treatment of port wine stain. For such an application, HMME has quite many advantages, such as stable structure, high singlet oxygen yield, strong photodynamic efficiency, low toxicity, and fast clearance.^{39,40} In this study, HMME is used as the sensitizer of TiO₂ NPs based on its advantage of visible light absorption. The combination of HMME and TiO₂ NP can help in enhancing white light absorption and hence daylight PDT efficiency.

2 Materials and Methods

TiO₂ NPs are obtained from the Capital Normal University (Beijing, China). HMME is purchased from Fudan Zhangjiang BioPharmaceutical Co. (Shanghai, China). It is dissolved in dimethyl sulfoxide (DMSO, Sigma Aldrich, St. Louis, Missouri), stored at room temperature, and then diluted as needed in ultrapure water or Dulbecco's modified eagle media (DMEM) (Gibco/BRL, Carlsbad, California). It has been reported that the amount of sensitizer linked onto TiO₂ NPs would affect the sensitizing efficiency.⁴¹ To determine the optimized linkage ratio for achieving the maximum sensitizing efficiency, HMME-TiO₂ NCs with different combination ratios are synthesized. HMME can be linked to TiO₂ NPs through the interaction between the anchoring carboxyl groups (COO⁻) of HMME and hydroxyl groups on the surface of TiO₂ NPs. The HMME-TiO₂ NC can also be formed through the interaction of anchoring carboxyl groups (COO⁻) directly with TiO₂.^{18,42–45} The chemical structure of HMME and the linking process are schematically shown in Fig. 1.

A stock solution of HMME with the concentration of 600 μg/mL is prepared by dissolving 0.012 g HMME in 2 mL DMSO and 18 mL ultrapure water. Also, a stock solution of 60,000 μg/mL TiO₂ NP is prepared by dissolving 1.22 g TiO₂ powder in 20 mL ultrapure water. HMME-TiO₂ NC samples with different combination ratios are synthesized by mixing different amounts of HMME with TiO₂ NP aqueous solution under sonication. The samples are then stirred in dark for 24 h at room temperature to form HMME-TiO₂ NCs.

The absorption spectra of HMME-TiO₂ NC samples are recorded using an ultraviolet-visible spectrophotometer (V-550 UV/VIS, JASCO, Japan). The crystal lattice structures of TiO₂ NP and HMME-TiO₂ NC are analyzed with x-ray diffraction (XRD) using an x-ray diffractometer (X'pert Powder, PANalytical B.V., Netherlands). The morphologies of the NP

and NC are studied with transmission electron microscopy (TEM) (JEM-2100, JEOL, Japan). Fluorescence spectra of HMME and HMME-TiO₂ NC, and DCF, which is produced when DCFH-DA (2',7'-dichlorodihydro-fluorescein diacetate) reacts with ROS for evaluating the ROS generation efficiency, are measured using a fluorescence spectrophotometer (F-4500, HITACHI, Japan). Fourier transform infrared spectroscopy (FT-IR) spectra are obtained using an infrared spectrometer (Vetex 70, Bruker, Germany). The powder samples of HMME, TiO₂ NP, and HMME-TiO₂ NC are individually mixed with KBr and then are pressed to form pellets for the FT-IR analysis. Hydrodynamic sizes of the particles are evaluated with the dynamic light scattering method (Zeta Sizer nano ZS90, Malvern, UK). Before the XRD and FT-IR measurements, the solution sample of HMME-TiO₂ NC is dried up to become a powder in a vacuum drying oven (DZF-6050, Beijing Zhongkehuanshi Instrument Co., Ltd., China).

Before cell experiment, the capability of HMME-TiO₂ NCs for generating ROS is evaluated with photocatalytic analysis through the photo degradation of methyl blue (MB) under irradiation. A xenon lamp with the emission spectral range of 380 to 700 nm for simulating solar irradiation is used as the light source. The distance between the lamp and the NC solution is 12 cm. For this measurement, HMME, TiO₂ NPs, and HMME-TiO₂ NCs with different combination ratios (the concentrations of TiO₂ NP in the TiO₂ NP and HMME-TiO₂ NC solutions are fixed at 7.5 mg/mL) of 6 mL are individually added to 6 mL MB aqueous solution (10 mg/L). The solution is irradiated after it is stirred in the dark for 2 h to accelerate MB adsorption. The residual concentration of MB is determined by measuring its absorption at 664 nm using the ultraviolet-visible spectrophotometer.

KB cells, which are obtained from The Fourth Military Medical University, Xi'an, China, are cultured in DMEM (high glucose, Gibco) medium with 10% (v/v) fetal bovine serum (Sijiqing, China) and 1% (v/v) penicillin streptomycin combination (Sigma) in a humidified standard incubator (HERA cell 150 Copper, Thermo Fisher Scientific) under 5% CO₂ atmosphere at 37°C. In an incubator, KB cells are seeded in 96-well plates at a density of ~1 × 10⁴ cells per well and cultured for 12 h in a complete medium. Then the medium is replaced by serum-free DMEM containing HMME, TiO₂ NPs, or HMME-TiO₂ NCs. Wells with cells are divided into different groups. In the control group, the cells are mock-treated (without drug or irradiation). In the photodynamic group, cells are incubated with HMME, TiO₂ NPs, or HMME-TiO₂ NCs and then illuminated by a xenon lamp. In the cytotoxicity group, cells are also incubated with HMME, TiO₂ NPs, or HMME-TiO₂ NCs,

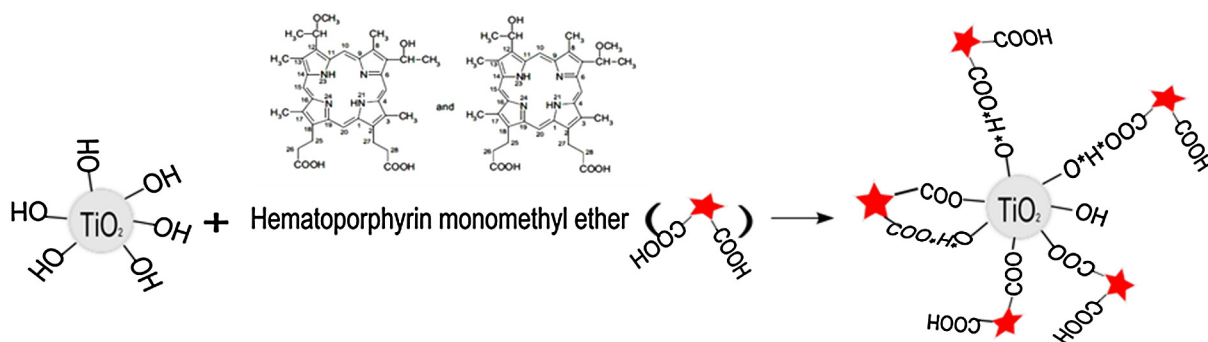


Fig. 1 Schematic demonstration of HMME conjugation onto TiO₂.

but no light irradiation is applied. The HMME-TiO₂ NCs with the concentrations of TiO₂ NP at 100, 200, and 400 $\mu\text{g}/\text{mL}$ and the combination ratio at 1 : 800 are used in this experiment. The concentrations of HMME used in this experiment are 0.125, 0.25, and 0.5 $\mu\text{g}/\text{mL}$. The concentrations of used pure TiO₂ NPs are also 100, 200, and 400 $\mu\text{g}/\text{mL}$. After incubation for 6 h, cell samples are washed twice with PBS and then fresh DMEM is added to the samples. In the photodynamic group, cells are irradiated with the xenon lamp for 5 min with a power density of 60 mW/cm². After irradiation, cells are incubated for another 12 h for viability evaluation. Cell viability is evaluated with the CCK-8 assay, in which 110 μL DMEM containing 10 μL CCK-8 (purchased from Dojindo, Japan) is added to the wells. The cells are then incubated for another 1 h at 37°C with 5% CO₂ for measuring the absorbance levels (OD values) at 450 nm using a microplate reader (Infinite M200 Pro., Tecan, Switzerland).

Generation of ROS is evaluated by using DCFH-DA as a probe. In the incubator, KB cells are seeded in 6-well plates at a density of 2.5×10^5 cells per well and incubated for 12 h in a complete medium. Then cells are incubated with DMEM containing HMME, TiO₂ NPs, or HMME-TiO₂ NCs with the combination ratio at 1 : 800 and the TiO₂ NP concentration at 400 $\mu\text{g}/\text{mL}$ for 6 h. The medium is then replaced by DMEM containing 10 μM DCFH-DA. Next, the cells are incubated for 30 min at 37°C. After that, cells are washed and irradiated with the xenon lamp for 5 min. The generated intracellular ROS can oxidize nonfluorescent DCFH-DA to become fluorescent DCF. Ten minutes after 5-min irradiation, microscopic images of KB

cells are recorded using Nikon eclipse Ti fluorescence microscope (Nikon, Japan). The fluorescence intensity at 535 nm is also monitored under the excitation of 485-nm light by using a fluorescence spectrophotometer. All statistical analyses are performed using SPSS18.0. Student's *t*-distribution test is utilized to compare the data obtained under different experimental conditions. *P*-values of <0.05 are considered to be significant.

3 Characterization Results of HMME-TiO₂ Nanocomposite

TEM analysis provides us with the information about the morphologies of TiO₂ NPs and HMME-TiO₂ NCs. Most TiO₂ NPs are sphere-like in shape with an average diameter around 10 nm. Some of them are aggregated, as shown in the TEM image of Fig. 2(a1). Such aggregations can be formed during the preparation of a specimen for TEM observation.⁴⁶ Figure 2(a2) shows the TEM image of a single TiO₂ NP. Figure 2(a3) shows the crystalline diffraction pattern of TiO₂. Figures 2(b1)–2(b3) and 2(c1)–2(c3) show the TEM analysis results similar to Figs. 2(a1)–2(a3), respectively, for the HMME-TiO₂ NCs with the combination ratios of 1 : 100 and 1 : 800, respectively. With such low combination ratios, the number of HMME molecule adsorbed onto a TiO₂ NP is small such that the morphology of an HMME-TiO₂ NC is similar to that of a TiO₂ NP. From Figs. 2(a3), 2(b3), and 2(c3), one can see that both TiO₂ NP and HMME-TiO₂ NC are in the anatase phase, indicating that the interaction of HMME and TiO₂ does not change the crystal structure of TiO₂. Anatase TiO₂ can have a higher catalytic

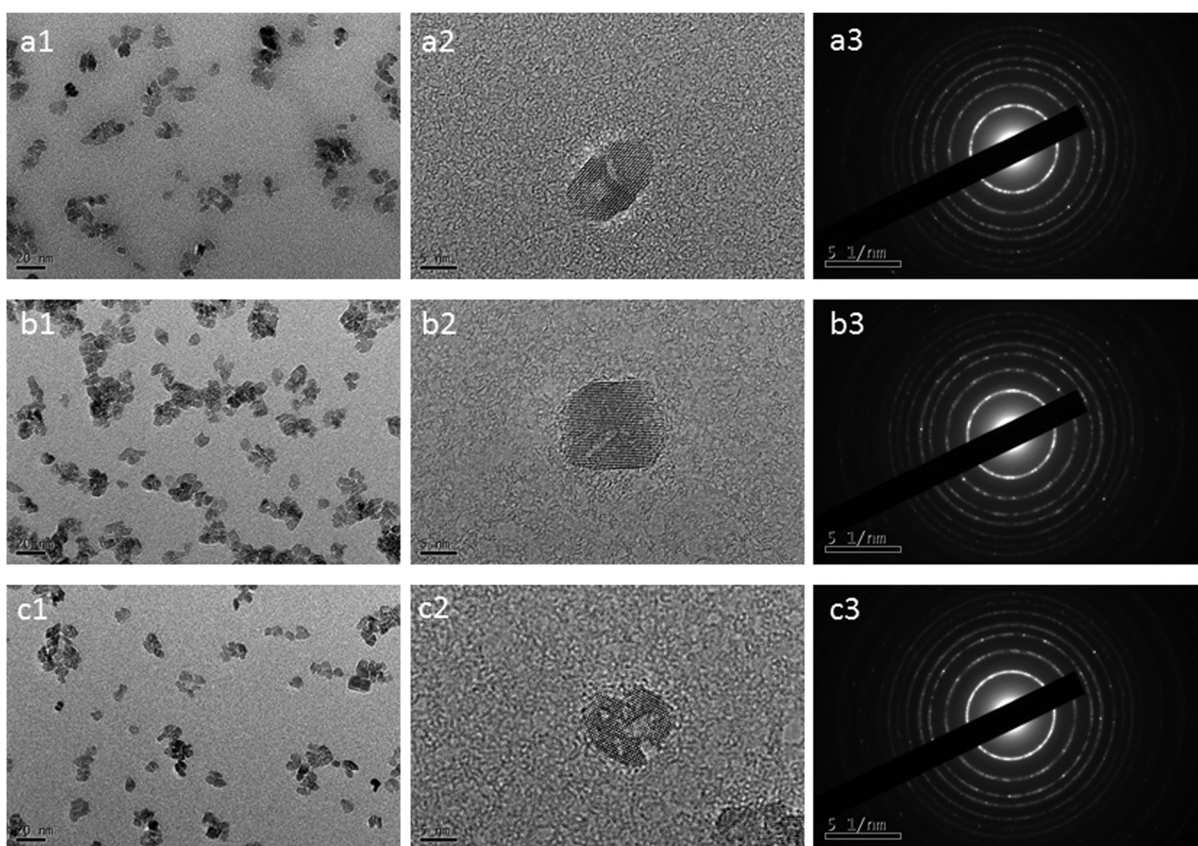


Fig. 2 TEM images (a1) and (a2) and crystalline diffraction pattern (a3) of TiO₂ NP. (b1)–(b3) and (c1)–(c3): TEM analysis results similar to (a1)–(a3) for the HMME-TiO₂ NCs with the combination ratios of 1 : 100 and 1 : 800, respectively.

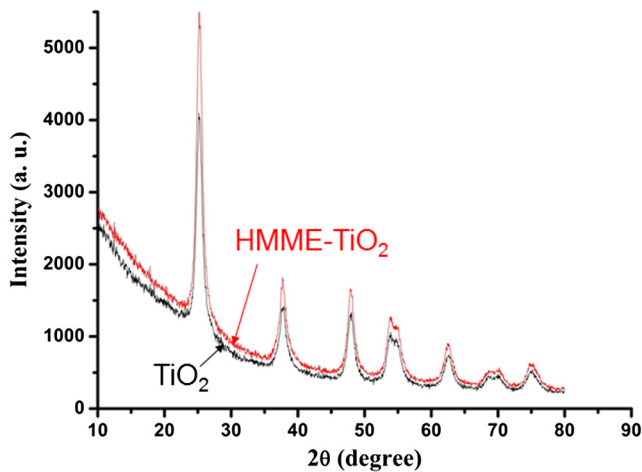


Fig. 3 XRD diffraction patterns of TiO₂ NP and HMME-TiO₂ NC.

activity when compared with the brookite or rutile structure. Figure 3 shows the XRD patterns of TiO₂ NP and HMME-TiO₂ NC (combination ratio at 1 : 1000) powders. The XRD patterns of both TiO₂ NP and HMME-TiO₂ NC exhibit consistent multiple sharp peaks in 2 θ scan at 25.3, 37.9, 48.0, 53.8, 55.1, and 62.7 deg, which confirm that the TiO₂ NP has the anatase structure.⁴¹ The results in Fig. 3 also indicate that the adsorption of HMME molecules onto TiO₂ NP does not change the crystal structure of TiO₂. According to Scherrer's equation, i.e., $D = 0.89\lambda/\beta \cos \theta$, we can estimate the sizes of TiO₂ NP and HMME-TiO₂ NC. Here, λ represents the wavelength of x-ray radiation (0.154 nm), β is the full-width at half-maximum of the most intense peak in the XRD diffraction pattern, and θ is the diffraction angle of the most intense peak (25.3 deg). The estimated sizes of TiO₂ NP and HMME-TiO₂ NC are 10.4 and 10.6 nm, respectively, indicating that the linkage of HMME onto a TiO₂ NP does not significantly change the size.

Figure 4 shows the UV-vis absorption spectra of HMME, TiO₂ NP, and HMME-TiO₂ NCs with various combination ratios. Here, one can see that the absorption of TiO₂ NP is quite strong in the deep-ultraviolet range and decays to almost zero in the visible range. HMME has an absorption peak around 380 nm and has a long absorption tail in the visible range. After the

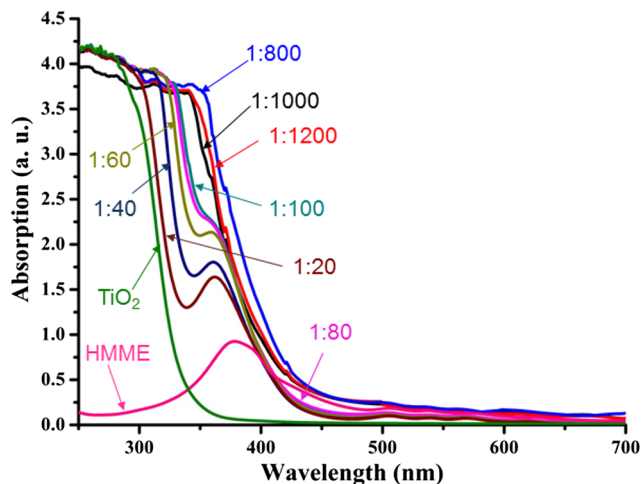


Fig. 4 UV-vis absorption spectra of HMME, TiO₂ NP, and HMME-TiO₂ NCs with various combination ratios.

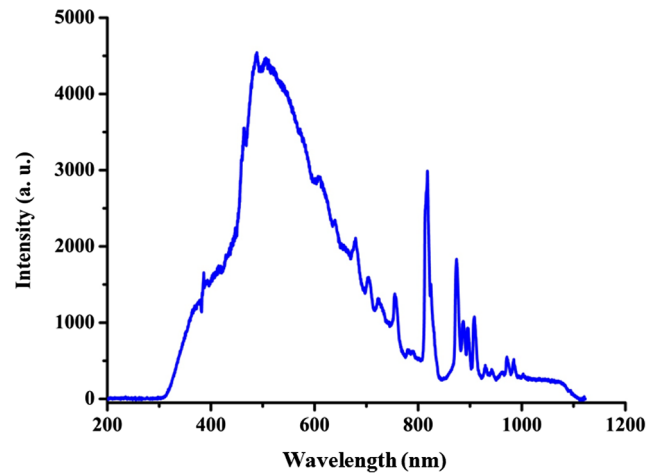


Fig. 5 Emission spectrum of the used xenon lamp.

adsorption of HMME onto TiO₂ NP, as x in the combination ratio 1 : x increases from 20 to 800 (decreasing HMME molecule number adsorbed onto a TiO₂ NP), the shoulder of TiO₂ absorption spectrum keeps red-shifting and merges with the HMME absorption peak, which blue shifts by ~ 17 nm after it is linked with TiO₂ NP. Meanwhile, although the absorption level of HMME in the visible range decreases after it is linked with TiO₂ NP, this level generally keeps increasing as x increases from 10 to 800. However, when x is further increased from 800, the shoulder of TiO₂ absorption spectrum starts to blue shift and the absorption level in the visible range starts to decrease. In other words, to maximize the absorption of the HMME-TiO₂ NC, the HMME molecule number adsorbed onto a TiO₂ NP cannot be too large or too small. The absorption of the HMME-TiO₂ NC in the emission spectral range of the xenon lamp is maximized when $x = 800$. The emission spectrum of the used xenon lamp is shown in Fig. 5. The absorption spectral variations described above in Fig. 4 are due to the complex formation between HMME and TiO₂ through the anchoring group ($-\text{COO}-$) of HMME.⁴⁷⁻⁴⁹

For further understanding, the interaction between the anchoring groups of HMME and TiO₂, FT-IR spectra of HMME, TiO₂ NP, and HMME-TiO₂ NC are analyzed. Figure 6 shows the FT-IR spectra of HMME (black line), TiO₂ NP (red line), and HMME-TiO₂ NC with the combination ratio at 1 : 800 (blue line). For HMME, the depressions around 1163 and 1610 cm^{-1} are caused by the stretching vibrations of the C-N and C=N bonds, respectively, in pyrrole. The other two depressions around 1547 and 3313 cm^{-1} are related to the stretching and bending vibrations of the N-H bond. The depression around 1703 cm^{-1} originates from the vibration of the anchoring group $-\text{COOH}$. For TiO₂, the characteristic features of $-\text{OH}$ are observed around 1624 and 3232 cm^{-1} . The broad and deep depression in the range from 800 to 450 cm^{-1} results from the vibration of the Ti-O bond.¹⁹ The characteristic vibration features of both HMME and TiO₂ can be observed in the FT-IR spectrum of HMME-TiO₂ NC, confirming the adsorption of HMME onto TiO₂ NP. Figure 7 shows the magnified portion of the FT-IR spectra in the spectral range of 1000 to 2000 cm^{-1} . Here, we can more clearly observe that the $-\text{COOH}$ vibration feature around 1703 cm^{-1} of HMME disappears. A depression feature appears around 1622 cm^{-1} after HMME is conjugated onto TiO₂. This feature is quite close to the TiO₂ feature at

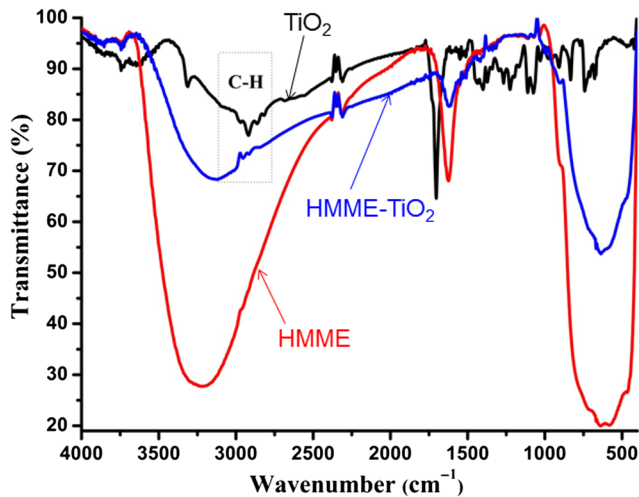


Fig. 6 FT-IR spectra of HMME, TiO₂ NP, and HMME-TiO₂ NC with the combination ratio at 1:800.

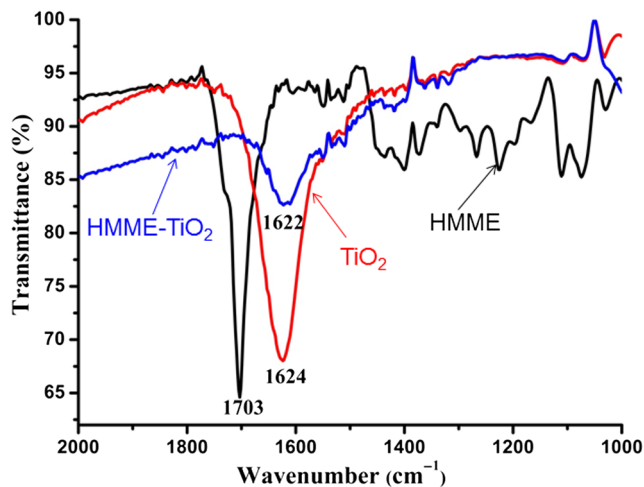


Fig. 7 FT-IR spectra of HMME, TiO₂ NP, and HMME-TiO₂ NC the same as those in Fig. 6 but in a smaller spectral range.

1624 cm⁻². The result again confirms that HMME is conjugated onto TiO₂ through the interaction between the -COOH anchoring groups in HMME and a TiO₂ NP.⁵⁰

Figure 8 shows the fluorescence spectra of HMME-TiO₂ NCs of different combination ratios with a fixed HMME concentration at 10 μg/mL. The results show that the HMME fluorescence is quenched when TiO₂ NP concentration increases. When the combination ratio of HMME-TiO₂ NC is 1:*x* with *x* > 10, the fluorescence of HMME is completely quenched. Similar fluorescence quenching behaviors of TCPP,⁴⁷ anthracene-9-carboxylic acid,⁵¹ and H2THPP⁵² by linked TiO₂ for solar cell applications have been reported. Such a behavior is caused by electron transfer from the excited state of the sensitizer into the conduction band of TiO₂. Under light irradiation, electrons transit from the ground state of HMME into its excited state. Electrons can then be transferred into the conduction band of TiO₂, leading to the quenching of HMME fluorescence.^{47,49,53}

The photocatalytic activity of HMME-TiO₂ NC indicates the capability of producing ROS under white light irradiation. The photocatalytic activities of TiO₂ NPs and HMME-TiO₂

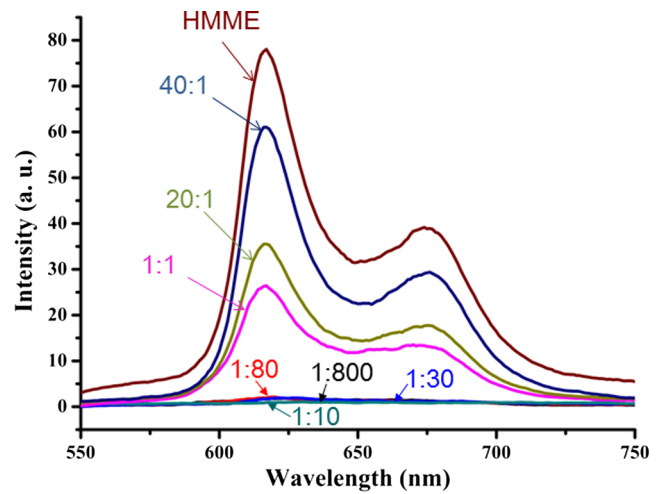


Fig. 8 Fluorescence spectra of HMME-TiO₂ NCs with different combination ratios.

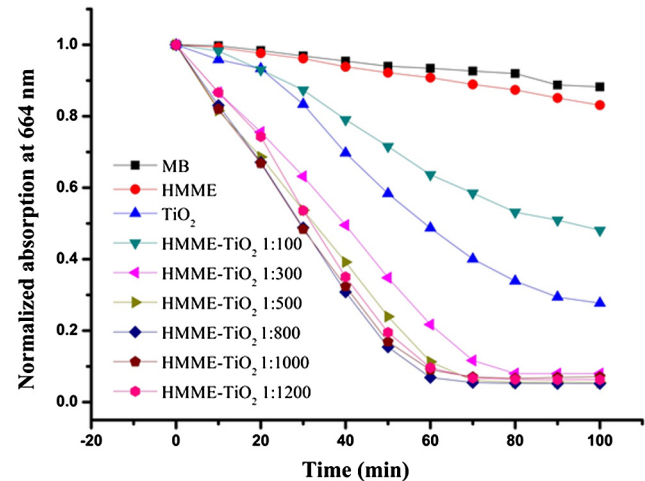


Fig. 9 Photocatalysis degradation of HMME, TiO₂ NP, and HMME-TiO₂ NCs with different combination ratios.

NCs with different combination ratios are examined with the photodegradation of MB under white light irradiation. The results are shown in Fig. 9. Here, the normalized absorption levels at 664 nm are shown as functions of irradiation time. Under xenon lamp irradiation, the photoactivity of HMME-TiO₂ NC with the combination ratio of 1:100 shows no difference from that of TiO₂ NP. When *x* of the combination ratio 1:*x* increases from 300 to 1200 (decreasing HMME molecule number adsorbed onto a TiO₂ NP), the photoactivity of HMME-TiO₂ NC first increases and then decreases. In particular, the degradation for the HMME-TiO₂ NC with the combination of 1:800 reaches 94% after 60 min irradiation. The results confirm that the amount of adsorbed HMME plays an important role in the sensitizing process.⁴⁴ From Fig. 9, one can see that HMME-TiO₂ NC with the combination ratio of 1:800 has the highest photoactivity. After 60-min irradiation, 94% MB is degraded by HMME-TiO₂ NC (1:800), whereas only 52% is degraded by TiO₂ NP. This result confirms that the photoactivity of TiO₂ NP under white light irradiation is significantly enhanced through the sensitization effect of HMME.

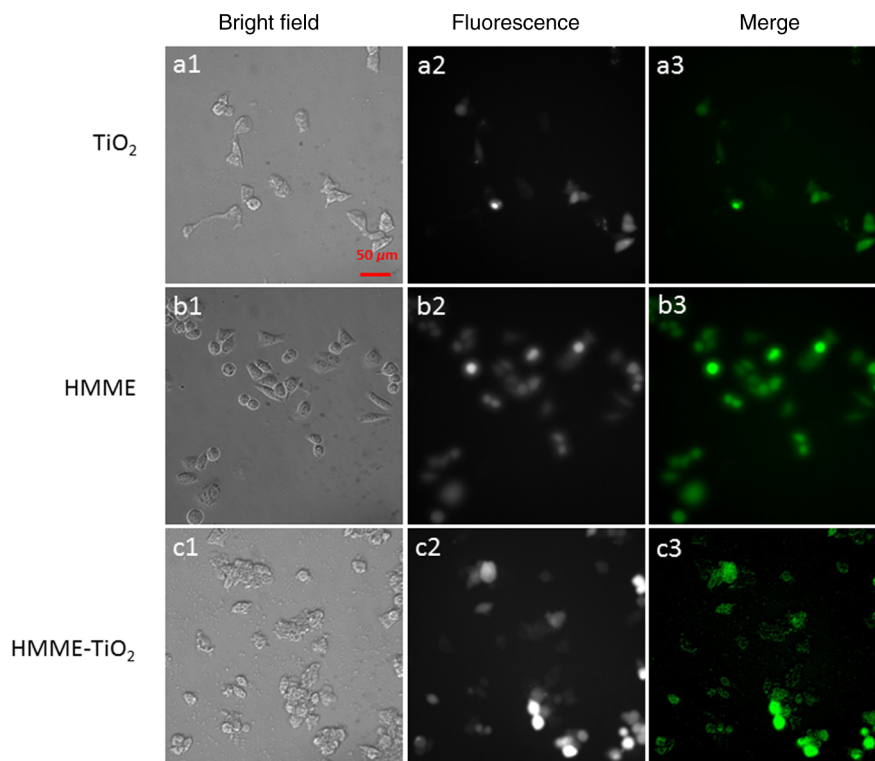


Fig. 10 Bright field [(a1)–(c1)], fluorescence [(a2)–(c2)] images, and their mergers [(a3)–(c3)] indicating the ROS generation in KB cells incubated with TiO₂ NPs, HMME, and HMME-TiO₂ NCs, respectively, under xenon lamp irradiation.

4 Application of HMME-TiO₂ Nanocomposite to Cancer Cell Inactivation

Intracellular ROS generation is the major cause for cell damage in the PDT process.⁵⁴ As shown in Figs. 10(a3)–10(c3), green fluorescence can be observed indicating that ROS is generated in the KB cells incubated with TiO₂ NPs, HMME, and HMME-TiO₂ NCs (1:800 in combination ratio), respectively, under xenon lamp irradiation. The fluorescence intensity in the cells incubated with HMME-TiO₂ NCs is stronger than those incubated with HMME or TiO₂ NPs. Figure 11 shows the calibrated fluorescence intensities under different incubation conditions revealing that a higher intracellular ROS level is observed in irradiated cells when they are incubated with HMME-TiO₂ NCs, when compared with cells incubated with HMME or TiO₂ NPs. HMME-TiO₂ NCs with the combination ratio of 1:800 is used to evaluate the photodynamic inactivation effect on KB cells under white light irradiation. The HMME-TiO₂ NCs, TiO₂ NPs, and HMME used in photodynamic experiments are diluted in DMEM to obtain the desired concentrations. Cells seeded in a 96-well plate are incubated with HMME, TiO₂ NP, and HMME-TiO₂ NC solutions for 6 h, followed by xenon lamp irradiation and then further incubation with fresh DMEM media for 24 h before cell viability measurement. The concentration of TiO₂ NP ranges from 100 to 400 μg/mL with the concentration of HMME (pure HMME or HMME in HMME-TiO₂ NC) varied from 0.125 to 0.5 μg/mL. In all cases, HMME and HMME-TiO₂ NC have the same HMME concentration, whereas TiO₂ NP and HMME-TiO₂ NC have the same TiO₂ NP concentration. As shown in Fig. 12, without light irradiation, the viability of KB cells incubated with TiO₂ NP, HMME, and HMME-TiO₂ NC of different concentrations is higher than 95%, indicating

that the cytotoxicity of HMME, TiO₂ NP, or HMME-TiO₂ NC is quite low. The good biocompatibility of HMME-TiO₂ NC makes it attractive for PDT application.

Figure 13 shows the viability of KB cells incubated with HMME, TiO₂ NP, and HMME-TiO₂ NCs after xenon lamp irradiation of 18 J/cm² in illumination dosage for 5 min. Here, the cell viability without TiO₂ NP or HMME remains almost 100% after irradiation (the case of irradiation only), indicating that the irradiation power level is harmless to the cells. However, the viability of cells treated with HMME, TiO₂ NPs, or

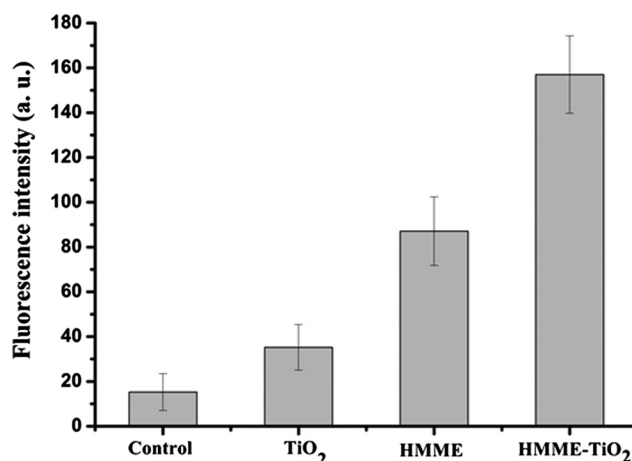


Fig. 11 Fluorescence intensities of DCF indicating the generated ROS levels in KB cells when they are incubated with TiO₂ NPs, HMME, and HMME-TiO₂ NCs.

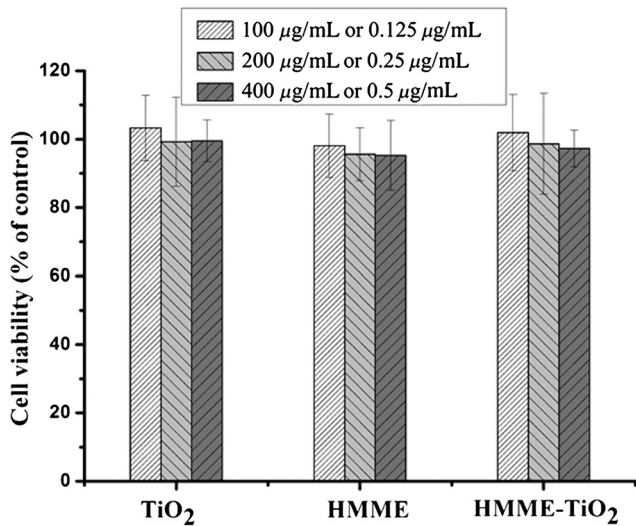


Fig. 12 Viability of KB cells treated with TiO₂ NPs, HMME, and HMME-TiO₂ NCs of different concentrations. No light irradiation is applied.

HMME-TiO₂ NCs decreases with increasing concentration. The viabilities of cells treated with TiO₂ NPs of different concentrations at 100, 200, and 400 µg/mL are 99.6%, 93.4%, and 88.7%, respectively. Those treated with HMME of different concentrations at 0.125, 0.25, and 0.5 µg/mL are 92.2%, 83.3%, and 55.3%, respectively. Thus, those treated with HMME-TiO₂ NCs (containing the same concentrations of HMME and TiO₂ NP as those of the HMME and TiO₂ NP groups, respectively) are 89.5%, 41.0%, and 15.3%, respectively. The high viability of cells treated with TiO₂ NPs after the irradiation for 5 min is due to the low absorption of TiO₂ NP in the visible range. It is noted that the photodynamic inactivation efficiency of HMME-TiO₂ NC on KB cells is higher than the efficiency summation of HMME and TiO₂ NP. This is attributed to the sensitizing effect of HMME on TiO₂ for effective ROS generation under the irradiation of visible light.

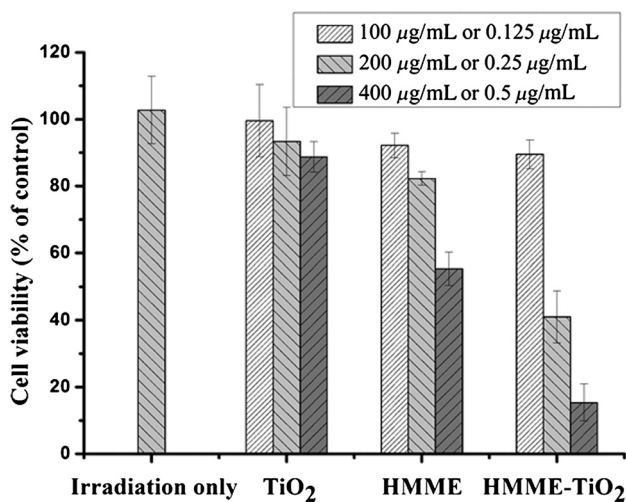


Fig. 13 Viability of KB cells treated with TiO₂ NPs, HMME, and HMME-TiO₂ NCs of different concentrations. Xenon lamp irradiation with the dosage of 18 J/cm² is applied.

5 Discussions

There are two mechanisms for the result that HMME-TiO₂ NC has a higher photocatalytic and PDT efficiency than that of HMME or TiO₂ NP. First, the absorption of HMME-TiO₂ NC in the visible range is enhanced when compared to TiO₂ NP. In other words, the irradiation of white light becomes more effective for PDT. Second, as schematically demonstrated in Fig. 14, TiO₂ NP is sensitized by HMME.^{47,49,51-53} Upon the excitation of visible light, electrons transit from the ground state of HMME into the singlet excited state, ¹[HMME]*. Some of the electrons can be relaxed from the singlet excited state into the triplet excited state, ³[HMME]*. In this situation, electrons can be transferred from ¹[HMME]* and ³[HMME]* excited states into the conduction band of TiO₂. Then the electrons can be trapped by the adsorbed O₂, resulting in the formation of ·O₂⁻, H₂O₂, and ·OH for the degradation of MB present on the surface of TiO₂ NP or the damage of cell structure. Such a process finally leads to the death of cancer cells.

In linking HMME onto TiO₂ NPs for effective TiO₂ sensitization and hence efficient ROS generation, the combination ratio of HMME-TiO₂ NC is a crucial factor. If the HMME molecule number adsorbed onto a TiO₂ NP is too small, the sensitization effect is low. However, if the HMME molecule number adsorbed onto a TiO₂ NP is too large, stacked HMME molecules on the surface of a TiO₂ NP result in an ineffective sensitization process. As shown in Fig. 4, when in the combination ratio of HMME-TiO₂ NC at 1 : x with x increasing from 10 to 800, the shoulder of the major absorption feature keeps red-shifting and the absorption level in the visible range keeps increasing. These results indicate that in this combination ratio range, the HMME molecule number adsorbed onto a TiO₂ NP is too large such that an increase of x (corresponding to a decrease of HMME molecular number on a TiO₂ NP) leads to higher absorption in the spectral range of the xenon lamp. However, when x becomes larger than 800, the shoulder of the major absorption feature blue-shifts and the absorption level in the visible range decreases, indicating that beyond this point, the HMME molecule number adsorbed onto a TiO₂ NP becomes too low and hence the sensitization effect decreases. Figure 8 shows that when x is larger than 10, the HMME fluorescence is completely quenched, confirming that the excited HMME energy is effectively transferred into TiO₂ when the HMME-TiO₂ combination ratio is 1 : 800. Then, in Fig. 9, we clearly show that the ROS generation efficiency of the HMME-TiO₂ NC with the combination ratio at 1 : 800 is highest among the samples of different combination ratios. This result is due to its efficient absorption, as shown in Fig. 4, and effective energy transfer from HMME into TiO₂, as shown in Fig. 8.

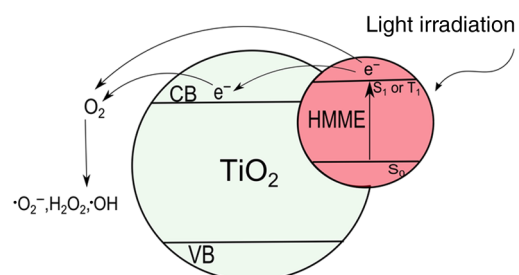


Fig. 14 Mechanism of the sensitization process of TiO₂ with HMME.

6 Conclusions

In summary, HMME has been conjugated onto TiO₂ NPs to obtain a higher PDT efficiency. HMME-TiO₂ NCs with different combination ratios were prepared and characterized with TEM, XRD, UV-vis, FT-IR, and fluorescence spectra. The results showed that HMME was successfully conjugated onto TiO₂ NP through the interaction between carboxyl and hydroxyl groups without changing the crystal structure of TiO₂. Photocatalytic degradation of MB demonstrated that HMME-TiO₂ NCs with the combination ratio of 1 : 800 had the strongest photocatalytic activity under xenon lamp irradiation. HMME-TiO₂ NC could generate more ROS and showed a higher photoinactivation effect on KB cells under xenon lamp irradiation. The result was attributed to two mechanisms. First, white light absorption of HMME-TiO₂ NC is higher than those of TiO₂ NP and HMME. Second, TiO₂ is sensitized by HMME leading to the effective generation of ROS under xenon lamp irradiation. Because the dark toxicity of HMME-TiO₂ NC is not higher than that of HMME, HMME-TiO₂ NC is expected to be useful for daylight PDT.

Disclosures

There is no relevant financial interest in the manuscript and no other potential conflict of interest to disclose.

Acknowledgments

This research was supported by the National Natural Science Foundation of China (Nos. 61361160413, 61335012, 61120106013, and 11274249). The TEM study was undertaken at the International Center for Dielectric Research (ICDR), Xi'an Jiaotong University, Xi'an, China. The authors also thank Mr. Chuansheng Ma for his help in using the TEM facility.

References

- S. B. Brown, E. A. Brown, and I. Walker, "The present and future role of photodynamic therapy in cancer treatment," *Lancet Oncol.* **5**(8), 497–508 (2004).
- S. Zhang and Z. Zhang, "5-aminolevulinic acid-based photodynamic therapy in leukemia cell HL60," *Photochem. Photobiol.* **79**(6), 545–550 (2004).
- S. Cherian and C. C. Wamser, "Adsorption and photoactivity of tetra (4-carboxyphenyl) porphyrin (TCPP) on nanoparticulate TiO₂," *J. Phys. Chem. B* **104**(15), 3624–3629 (2000).
- C. Y. Lee and J. T. Hupp, "Dye sensitized solar cells: TiO₂ sensitization with a bodipy-porphyrin antenna system," *Langmuir* **26**(5), 3760–3765 (2010).
- M.-Y. Chang et al., "Photocatalytic degradation of 2, 4-dichlorophenol wastewater using porphyrin/TiO₂ complexes activated by visible light," *Thin Solid Films* **517**(14), 3888–3891 (2009).
- X.-T. Zhou, H.-B. Ji, and X.-J. Huang, "Photocatalytic degradation of methyl orange over metalloporphyrins supported on TiO₂ degussa P25," *Molecules* **17**(2), 1149–1158 (2012).
- H. Imahori et al., "Photoinduced charge carrier dynamics of Zn-porphyrin-TiO₂ electrodes: the key role of charge recombination for solar cell performance," *J. Phys. Chem. A* **115**(16), 3679–3690 (2011).
- M.-M. Yu et al., "Preparation, characterization, and photocatalytic properties of composite materials of copper (II) porphyrin/TiO₂," *J. Mater. Sci.* **49**(16), 5519–5528 (2014).
- X. Liu et al., "Solvothermal preparation of copper (II) porphyrin-sensitized mesoporous TiO₂ composites: enhanced photocatalytic activity and stability in degradation of 4-nitrophenol," *Res. Chem. Intermed.* **42**(6), 5197–5208 (2016).
- H. You and Y. Zhao, "Synthesis, characterization and visible photocatalytic performance of Iron (III) tetracarboxyphthalocyanine-sensitized TiO₂ photocatalyst," *J. Phys. Chem. Biophys.* **6**(1), 1000199 (2016).
- T. Paunesku et al., "Biology of TiO₂-oligonucleotide nanocomposites," *Nat. Mater.* **2**(5), 343–346 (2003).
- C. Zhao et al., "Titanium dioxide-tetra sulphonatophenyl porphyrin nanocomposites for target cellular bio-imaging and treatment of rheumatoid arthritis," *Sci. China Chem.* **59**(5), 637–642 (2016).
- K. Huang et al., "The photocatalytic inactivation effect of Fe-doped TiO₂ nanocomposites on leukemic HL60 cells-based photodynamic therapy," *Int. J. Photoenergy* **2012**, 367072 (2012).
- N. Miyoshi et al., "Application of titanium dioxide (TiO₂) nanoparticles in photodynamic therapy (PDT) of an experimental tumor," in *The 4th Nanoscience and Nanotechnology Sanotechnology Symp. (NNS2011): An Int. Symp.*, Vol. **1415**, pp. 21–23, AIP Publishing (2011).
- L. Chen, M.-X. Liao, and J.-W. Xiong, "Experiment research of the vivo destruction of HL60 cells by use of TiO₂ and iron-doped TiO₂-based photodynamic therapy," *J. Optoelectron. Laser* **19**(2), 278–281 (2008).
- S. Yamaguchi et al., "Novel photodynamic therapy using water dispersed TiO₂ polyethylene glycol compound: evaluation of antitumor effect on glioma cells and spheroids in vitro," *Photochem. Photobiol.* **86**(4), 964–971 (2010).
- C. Wang et al., "Induction of cytotoxicity by photoexcitation of TiO₂ can prolong survival in glioma-bearing mice," *Mol. Biol. Rep.* **38**(1), 523–530 (2011).
- C. Zhao et al., "Bio-imaging and photodynamic therapy with tetra sulphonatophenyl porphyrin (TSPP)-TiO₂ nanowhiskers: new approaches in rheumatoid arthritis theranostics," *Sci. Rep.* **5**, 11518 (2015).
- T. Lopez et al., "Study of the stabilization of zinc phthalocyanine in sol-gel TiO₂ for photodynamic therapy applications," *Nanomed. Nanotechnol. Biol. Med.* **6**(6), 777–785 (2010).
- Z. Hou et al., "UV-emitting upconversion-based TiO₂ photosensitizing nanoplatform: near-infrared light mediated in vivo photodynamic therapy via mitochondria-involved apoptosis pathway," *ACS Nano* **9**(3), 2584–2599 (2015).
- L. Zeng et al., "Doxorubicin-loaded NaYF₄:Yb/Tm-TiO₂ inorganic photosensitizers for NIR-triggered photodynamic therapy and enhanced chemotherapy in drug-resistant breast cancers," *Biomaterials* **57**, 93–106 (2015).
- Z. Yu et al., "A near-infrared triggered nanophotosensitizer inducing domino effect on mitochondrial reactive oxygen species burst for cancer therapy," *ACS Nano* **9**(11), 11064–11074 (2015).
- W. Ren et al., "A near infrared light triggered hydrogenated black TiO₂ for cancer photothermal therapy," *Adv. Healthcare Mater.* **4**(10), 1526–1536 (2015).
- L. Pérez-Pérez, J. García-Gavín, and Y. Gilaberte, "Daylight-mediated photodynamic therapy in Spain: advantages and disadvantages," *Actas Dermo-Sifiliogr.* **105**(7), 663–674 (2014).
- K. Togsverd-Bo et al., "Artificial daylight photodynamic therapy with 'non-inflammatory' doses of hexyl aminolevulinic acid only marginally delays SCC development in UV-exposed hairless mice," *Photochem. Photobiol. Sci.* **12**(12), 2130–2136 (2013).
- J. Strasswimmer and D. J. Grande, "Do pulsed lasers produce an effective photodynamic therapy response?" *Lasers Surg. Med.* **38**(1), 22–25 (2006).
- R. Batchelor, G. Stables, and M. Stringer, "Successful treatment of scalp actinic keratoses with photodynamic therapy using ambient light," *Br. J. Dermatol.* **156**(4), 779–781 (2007).
- S. Wiegell et al., "Photodynamic therapy of actinic keratoses with 8% and 16% methyl aminolaevulinic acid and home-based daylight exposure: a double-blinded randomized clinical trial," *Br. J. Dermatol.* **160**(6), 1308–1314 (2009).
- S. Wiegell et al., "Daylight photodynamic therapy for actinic keratosis: an international consensus," *J. Eur. Acad. Dermatol. Venereol.* **26**(6), 673–679 (2012).
- S. Wiegell, V. Skødt, and H. Wulf, "Daylight-mediated photodynamic therapy of basal cell carcinomas-an explorative study," *J. Eur. Acad. Dermatol. Venereol.* **28**(2), 169–175 (2014).
- S. Wiegell et al., "Continuous activation of PpIX by daylight is as effective as and less painful than conventional photodynamic therapy for actinic keratoses: a randomized, controlled, single-blinded study," *Br. J. Dermatol.* **158**(4), 740–746 (2008).
- A. L. Linsebigler, G. Q. Lu, and J. T. Yates, "Photocatalysis on TiO₂ surfaces-principles, mechanisms, and selected results," *Chem. Rev.* **95**(3), 735–758 (1995).

33. J. Xu et al., "Photokilling cancer cells using highly cell-specific antibody-TiO₂ bioconjugates and electroporation," *Bioelectrochemistry* **71**(2), 217–222 (2007).
34. K. Cheng et al., "Magnetic antibody-linked nanomatchmakers for therapeutic cell targeting," *Nat. Commun.* **5**, 4880 (2014).
35. P. Xu et al., "A new strategy for TiO₂ whiskers mediated multi-mode cancer treatment," *Nanoscale Res. Lett.* **10**(1), 1–11 (2015).
36. Y. H. Tsuang et al., "Studies of photokilling of bacteria using titanium dioxide nanoparticles," *Artif. Organs* **32**(2), 167–174 (2008).
37. M.-Y. Duan et al., "Photocatalytic activity of novel tin porphyrin/TiO₂ based composites," *J. Phys. Chem. C* **114**(17), 7857–7862 (2010).
38. W. Kim et al., "Visible light photocatalysts based on homogeneous and heterogenized tin porphyrins," *J. Phys. Chem. C* **112**(2), 491–499 (2008).
39. Z. Huang, "Photodynamic therapy in China: over 25 years of unique clinical experience: part two—clinical experience," *Photodiagn. Photodyn. Ther.* **3**(2), 71–84 (2006).
40. X. Ding et al., "Hematoporphyrin monomethyl ether photodynamic damage on HeLa cells by means of reactive oxygen species production and cytosolic free calcium concentration elevation," *Cancer Lett.* **216**(1), 43–54 (2004).
41. R. B. Koehorst et al., "Spectral sensitization of TiO₂ substrates by monolayers of porphyrin heterodimers," *J. Phys. Chem. B* **104**(10), 2371–2377 (2000).
42. C. Huang et al., "Visible photocatalytic activity and photoelectrochemical behavior of TiO₂ nanoparticles modified with metal porphyrins containing hydroxyl group," *Ceram. Int.* **40**(5), 7093–7098 (2014).
43. T. Rajh et al., "Titanium dioxide in the service of the biomedical revolution," *Chem. Rev.* **114**(19), 10177–10216 (2014).
44. A. S. Hart et al., "Porphyrin-sensitized solar cells: effect of carboxyl anchor group orientation on the cell performance," *ACS Appl. Mater. Interfaces* **5**(11), 5314–5323 (2013).
45. F. Odobel et al., "Porphyrin dyes for TiO₂ sensitization," *J. Mater. Chem.* **13**(3), 502–510 (2003).
46. W. F. Vevers and A. N. Jha, "Genotoxic and cytotoxic potential of titanium dioxide (TiO₂) nanoparticles on fish cells in vitro," *Ecotoxicology* **17**(5), 410–420 (2008).
47. A. Kathiravan and R. Renganathan, "Effect of anchoring group on the photosensitization of colloidal TiO₂ nanoparticles with porphyrins," *J. Colloid Interface Sci.* **331**(2), 401–407 (2009).
48. M. Hilgendorff and V. Sundström, "Dynamics of electron injection and recombination of dye-sensitized TiO₂ particles," *J. Phys. Chem. B* **102**(51), 10505–10514 (1998).
49. S. Afzal, W. A. Daoud, and S. J. Langford, "Photostable self-cleaning cotton by a copper (II) porphyrin/TiO₂ visible-light photocatalytic system," *ACS Appl. Mater. Interfaces* **5**(11), 4753–4759 (2013).
50. I. A. Jankovic et al., "Surface modification of colloidal TiO₂ nanoparticles with bidentate benzene derivatives," *J. Phys. Chem. C* **113**(29), 12645–12652 (2009).
51. P. V. Kamat, "Photoelectrochemistry in particulate systems. 9. Photosensitized reduction in a colloidal titania system using anthracene-9-carboxylate as the sensitizer," *J. Phys. Chem.* **93**(2), 859–864 (1989).
52. S. Millesi et al., "Photoexcited porphyrins functionalizing TiO₂ and SnO₂ nanocrystals," *J. Phys. Chem. C* **119**(41), 23743–23751 (2015).
53. T. Ma et al., "Photoelectrochemical properties of TiO₂ electrodes sensitized by porphyrin derivatives with different numbers of carboxyl groups," *J. Electroanal. Chem.* **537**(1), 31–38 (2002).
54. M. V. Gozali et al., "Photodynamic therapy inhibit fibroblast growth factor-10 induced keratinocyte differentiation and proliferation through ROS in fibroblast growth factor receptor-2b pathway," *Sci. Rep.* **6**, 27402 (2016).

Biographies for the authors are not available.